DOI: https://doi.org/10.2138/am-2020-7131. http://www.minsocam.org/

Revision 2

American Mineralogist

Characterizing Low-Temperature Aqueous Alteration of Mars-Analog Basalts from Mauna Kea at Multiple Scales

Brandon P. Rasmussen[1,*], Wendy M. Calvin[1], Bethany L. Ehlmann[2,5], Thomas F. Bristow[3], Nicole Lautze[4], Abigail A. Fraeman[5] , Joel W. DesOrmeau[1]

[1] Department of Geological Sciences, University of Nevada, Reno, NV 89577, USA

[2] Division of Geological and Planetary Sciences, California Institute of Technology, Pasadena, CA 91125, USA

[3] NASA Ames Research Center, Moffett Field, CA 94035, USA

[4] School of Ocean and Earth Science and Technology, University of Hawaii at Manoa, Honolulu, HI 96822, USA

[5] Jet Propulsion Laboratory, California Institute of Technology, Pasadena, CA 91109, USA

[*] E-mail: brasmuss@caltech.edu

Abstract

We performed a multi-scale characterization of aqueous alteration of Mars analog basaltic rock from a Mauna Kea drill core using high-resolution visible and short-wave infrared (VIS-SWIR) spectral imaging, scanning electron microscopy, X-ray diffraction, and point VIS-SWIR spectra. Several types of smectites, zeolites, and primary minerals were identified. Mineral classes were mapped in cut sections extracted from the drill core and used to represent the range of alteration products seen in field data collected over 1000m depth (Calvin et al., in press). Ten distinct spectral endmembers identified in the cut sections were used to map the field point spectra. Trioctahedral Fe- and Mg-rich smectites were present towards the top of the zone of analysis (972 m below the surface) and increased in abundance towards the bottom of the drill core (1763 m depth). The mineralogy demonstrates a general trend of discontinuous alteration that increases in intensity with depth, with less pervasive phyllosilicate alteration at the top, several zones of different mixtures of zeolites towards the center, followed by more abundant phyllosilicates in the lowest sections. Distinctly absent are Fe-Mg phyllosilicates other than smectites, as well as carbonates, sulfates, and Al phyllosilicates such as kaolinite or illite. Furthermore, hematite was only detected in two of 24 samples. The suite of assemblages points to aqueous alteration at low to moderate temperatures at neutral to basic pH in low-oxygen conditions, with little evidence of extensive surface interaction, presenting a possible analog for an early Mars subsurface environment. We also present a library of VIS-SWIR spectra of the analyzed cut sections including both spatial averages (i.e., unweighted linear mixtures) of spectral images of each cut section and single point spectra of the cut sections. This will allow for consideration of nonlinear mixing effects in point spectra of these assemblages from natural surfaces in future terrestrial or planetary work.

Keywords: visible to short-wave infrared spectroscopy, X-ray diffraction, scanning electron microscopy, Mars analog, natural zeolites, Mg/Fe smectites, aqueous alteration

Introduction

VIS-SWIR spectroscopy can detect absorptions of most aqueous alteration minerals and many primary minerals that result from a variety of processes and thus provides valuable mineralogical information. Zeolites are identified by vibrational absorptions associated with H_2O near 0.97, 1.40, and 1.90 μm while smectites are identified by combinations of H_2O (1.40, 1.90 μm), OH (~1.40 μm), and several metal-OH combination bands, which vary in position from ~2.20-2.32 μm based on composition and structure (e.g. Clark, 1990a). Pyroxenes, iron oxides, and olivine are identified by broad absorptions related to electronic processes involving electrons in Fe and their energy state transitions (e.g. Hunt, 1977). However, overlapping or similar vibrational absorption features of mineral phases are common, so other methods are often required to provide complete mineralogical characterization; this is especially true for mineral assemblages. The absorptions discussed in this paper are well documented and library spectra are available from the USGS (Clark, 1990a; Kokaly et al., 2017), though modifications of these absorptions by compositional and structural differences is still an active area of study.

With the Compact Reconnaissance Imaging Spectrometer for Mars (CRISM) instrument aboard the Mars Reconnaissance Orbiter (MRO), orbital VIS-SWIR spectra achieved the unprecedented resolution at Mars of 18m/pixel in targeted mode. This resolution allows for interpretations of single, outcrop-sized areas and for more robust inspection of lower-concentration minerals (Murchie et al., 2007). Multiple recent papers by the CRISM team and their collaborators revealed that Martian secondary alteration is both spatially and temporally heterogeneous (e.g., Ehlmann and Edwards, 2014). Several different phases that formed from aqueous alteration have been studied in hundreds of locations on Mars, and genetic alteration mechanisms have been suggested to range from impact and shock generated material, to low-temperature metamorphism or hydrothermal activity, to neutral or acidic ground or surface water interaction (e.g., Bishop et al., 2008; Ehlmann et al., 2011a,b; Catalano, 2013; Tornabene et al., 2013; Michalski et al., 2013; Carter et al., 2013; Cannon et al., 2017; Carrozzo et al., 2017). Specific phases tied to these genetic origins by Mars analog work on Earth are hydrated silicates, carbonates, phyllosilicates, Fe-oxides, and sulfates, all of which have been spectrally identified on Mars from orbit and ground truthed by rovers (e.g., Bibring et al., 2006; Ehlmann et al., 2009; Morris et al., 2010; Ehlmann and Edwards, 2014; Arvidson et al., 2014; Vaniman et al., 2014; Rampe et al., 2017).

These alteration minerals provide evidence for occurrences of specific surface and subsurface processes on Mars, many of which can produce environments habitable for microbial life. A challenge is deciphering what environmental conditions the mineral assemblages on Mars represent, especially for common phases like Fe/Mg smectites, which can form in multiple environments. Through laboratory measurements of analog samples, we can observe the spectral properties of mineral assemblages, identify specific constituent alteration minerals and their spectral properties, and use these data to provide constraints on their environments of formation. This allows for comparison with spectra from Mars with implications for better understanding alteration in Martian environments. Here, we examine rock from drill core into Hawaiian basalts. These mafic flows were sequentially erupted onto the surface and later altered by water and provide an analog for aqueous alteration processes in the subsurface of ancient Mars. We utilize VIS-SWIR spectroscopy, X-ray diffraction (XRD), and scanning electron microscopy on cut sections of core and relate the spectral properties back to the field spectral data.

Previous Martian Analog Alteration Studies

There have been many terrestrial analog studies of natural, Mars-relevant alteration phases and mineral assemblages to help identify secondary minerals and interpret environments on Mars. Many studies focus on the alteration of basalt and the formation of smectite because Mars is primarily basaltic and smectite is a common secondary mineral. In-depth spectral and geochemical analyses of an analog Martian smectite similar to one observed in situ at Gale Crater were carried out by Treiman et al. (2014). This ferrian saponite exhibited a similar XRD pattern to a smectite studied in-situ at Yellowknife Bay using the CheMin instrument onboard the Mars Science Laboratory, suggesting that most of the octahedral Fe^{2+} in the Martian smectite had similarly been oxidized to Fe^{3+}. However, geological context of the studied samples is not well-defined as the samples were gathered at a field location which is no longer accessible. The saponite is thought to have formed diagenetically in a marine environment as a vesicle fill in basalt (Treiman et al., 2014), so the formation environment is not identical to that of the lacustrine mudstone at Yellowknife Bay (Grotzinger et al., 2014).

Many Mars analog studies have been focused on minerals at the surface or near surface and have inspected surface hydrothermal systems, impact sites, or groundwater-facilitated alteration that has been exposed to the surface environment through erosion (e.g., Bishop and Murad, 2002; Greenberger et al., 2012; Ehlmann et al., 2012; Hadnott et al., 2017). Mauna Kea has been studied in the near surface environment by both remote sensing and field methods (e.g., Morris et al., 2005; Guinness et al., 2007; McCanta et al., 2014), and palagonitic tephra from Mauna Kea's surface has been used for decades as a Mars soil simulant since early work identified it as spectrally similar to bright regions on Mars (Morris et al., 1990). We probe a less-studied part of the volcanic stratigraphy and note a different suite of mineral assemblages than in surface exposures.

Studying synthetic Mars analog minerals is also valuable for interpreting ancient aqueous environments on Mars and identifying likely formation conditions. Chemtob et al. (2015) characterized synthetic trioctahedral smectites both chemically and spectrally, and oxidation effects on the VIS-SWIR spectra and XRD patterns of smectites were studied by Chemtob et al. (2017). Chemtob et al. (2017) demonstrated that the abundant ferrian smectites observed from orbital data could be formed from oxidation of ferrous smectites. The formation of synthetic Fe-Mg smectites in oxidizing conditions was examined by Gainey et al. (2017); results showed that both dioctahedral and trioctahedral phases could form in basic, oxygen-rich conditions, given the presence of Fe^{3+} and either Mg^{2+} or Fe^{2+}. However, Viennet et al. (2017) showed that while pH has little influence on saponite formation, the presence of zeolites implies pH ~> 7.2, and increasing acidity implies more trioctahedral chlorite formation versus saponite. These studies illustrate that characterizing the entire secondary mineral assemblage is necessary for understanding early Martian geochemical and atmospheric conditions.

Our methodology is derived from a combination of approaches that have worked well in the past for identifying secondary minerals. Field-collected point-spectra provide a rapid characterization of bulk alteration mineralogy changes and are compared with more traditional, time consuming methods such as XRD, optical microscopy, and geochemical analyses (Calvin and Pace, 2016). This allows for targeting areas of interest for examining small scale spatial relationships through petrographic thin section work (see Calvin et al., in press) and spectral imaging and directly comparing spectral data with compositional information from scanning electron microscopy (Greenberger et al., 2015; Leask and Ehlmann, 2016). Bulk and clay-fraction XRD then allows for identification of species which are spectrally and/or compositionally similar.

This analysis contributes a unique study of alteration of basalts in a subsurface environment sheltered from direct atmospheric or seawater interaction and combines multiple methods to observe small-scale and large-scale distributions, macro and microscopic textural and spectral information, and mineral associations as a Mars analog. We then tie the interpretations of formation conditions back to specific VIS-SWIR absorption features to allow for broad applicability to other studies with the fast, non-destructive method of VIS-SWIR spectroscopy.

HGRP Samples and Geologic Context

The Humu'ula Groundwater Research Project (HGRP) drilled the continuously-cored hole PTA-2 in the saddle region of the Big Island of Hawaii in 2013, searching for groundwater resources. The core traverses much of the shield building phase of Mauna Kea, intersecting variably textured basaltic lava flows, explosive units, intrusive units, and sedimentary units. This study focuses on the basaltic lava portions of the stratigraphy, which make up the majority (>90%) of the core. Jerram et al. (2019) describe wireline logging and imaging of PTA-2. Calvin et al. (in press) further describe the geologic setting and drilling history for the study samples. As described in that paper, initial field measurements collected 780 VIS-SWIR point spectra over 791m, yielding eight distinct spectral types representing mineral assemblages at spot sizes of 1.5cm in diameter. These were used to select 25 cut sections that were subject to additional analyses as described in this work (one cut section was too small for XRD analysis). The eight spectral endmembers included primary mafic minerals (augite and augite with olivine) and alteration minerals, which included three types of phyllosilicates and three types of zeolites.

Methods

Spectral Data Collection

Twenty-five small (~2x3 cm) cut sections were measured with the same point spectrometer used in the preliminary study (Calvin et al., in press), and eight samples were selected for measurement at the Jet Propulsion Laboratory (JPL) with the Ultra Compact Imaging Spectrometer (UCIS) (Van Gorp et al., 2014). These eight samples were chosen as discussed by Calvin et al. based on petrographic analysis of thin sections and the field spectral survey, which concluded that the breadth of aqueous alteration mineralogy of the core was well represented across these eight samples.

Through the use of different front optics, the UCIS spectrometer can operate in either a telescopic or microscopic imaging mode suitable for analyzing meter-scale outcrops in the field or centimeter-scale laboratory samples, respectively. In the microimaging mode utilized in this study, UCIS collects spectra from samples at 81 μm/pixel across 213 discrete wavelengths from 0.5 – 2.5 μm (roughly the same range as the field-collected point spectra). The spectral resolution is approximately 10 nm. A single scan over a ~3 cm x 3 cm area takes ~1 minute to complete. A spectralon calibration target placed on the stage is used to calibrate each cut section image to reflectance. The sample spectrum is divided by the calibration target spectrum and multiplied by the spectral properties of spectralon to obtain an absolute reflectance. Due to low signal-to-noise ratio (SNR) from generally low albedo targets at very high spatial resolution, all UCIS images were averaged 3x3 spatially to improve spectral mapping capabilities, resulting in an effective pixel size of ~240 μm for images used in this study.

Spectral Matching Methods

Micro-imaging spectroscopy was used to obtain a mineral map of the entire surface of each of the eight samples. First, spectral variability and resulting endmember minerals and mineral mixtures were identified via the three preliminary spectral data products (spectral angle, decorrelation stretch, feature fitting) discussed in the following paragraphs. These in-scene endmembers (Figure 1) were then used to produce the final mineral maps (true color images in Figure 2, final maps in Figure 3), and multiple depth profile “images” of the core from the 780 field spectra (Figure 4).

Initial spectral matching and all following mapping methods were performed using the ENVI software package on both the micro-imaging spectroscopy dataset, and the 780 field-collected point spectra. The eight, spatially downsampled UCIS cut sections were mosaicked together into a single image, and the endmembers identified from the field data (Calvin et al., in press) were used as an initial set of spectra to classify the UCIS images. Spectral angle mapping (SAM) of the 1.70-2.45 μm region, and decorrelation stretching (DCS) of channels at 1.70, 1.91, and 2.15 μm were performed to observe spectral variability and extract initial spectral endmembers from the cut sections. SAM is a commonly used method in imaging spectroscopy in which each pixel is represented as a vector and the angle between reference spectra and each pixel is calculated as a measure of similarity. DCS removes inter-band correlation between selected channels by stretching principal component values before an inverse transform, and emphasizes spatial variability (Campbell, 1996). Endmember spectra from the samples were compared to spectra from the USGS spectral library (Kokaly et al., 2017) that had been resampled to UCIS wavelengths. The one phyllosilicate endmember without a good match in the USGS library was identified via decorrelation stretching and extracted from UCIS data. After resampling the USGS spectra to the same wavelengths as the UCIS spectra, spectral feature fitting (SFF) was performed using the USGS spectra and the one unique UCIS spectrum as reference data. SFF fits continuum-removed target spectra to continuum-removed pixels in the image, using a least squares optimization (Clark 1990b). The algorithm was originally designed for fitting single, complex features but has been shown to be effective across multiple features (Clark et al., 1991). The RMSE between the best-fit reference spectrum and the pixel is then thresholded to produce a classified image.

Final mapping was guided using a combination of these three data products (SAM, DCS, and USGS-spectra SFF), and compositional information gained from scanning electron microscopy (SEM). Mineral identification of the spectral endmembers was guided by comparison to USGS library spectra, EDS-derived data, and other published spectral data.

Spectral Mapping

Final mapping of the cut sections was accomplished using SFF and in-scene pixels from UCIS data as targets. This was because the USGS library spectra lacked representative secondary absorption features. These features included broad absorptions in the visible and near-infrared (VNIR) for phyllosilicates due to Fe absorptions and compositionally dependent SWIR features not represented in the library (i.e., the 2.245 μm absorption in one endmember discussed later) (Figure 1). Two specific endmembers are also identified as mixtures (Figure 1) and thus have no representative match in the USGS library.

Unlike in the initial SAM, where a single angle tolerance was applied to all images, different RMSE tolerances and wavelength-mapping ranges were used to specifically target wavelength ranges most characteristic of specific minerals for SFF. The zeolites were mapped using features within the 0.9-2.15 μm range, the phyllosilicates within the 1.30-2.45 μm range, and the primary mafic minerals within the 0.5-1.70 μm range. In the case of a fibrous zeolite identified with the SEM in the SR-618 cut section, pixels were hand-selected for the class as the UCIS signal was too low to result in a good automated match. Spectral imaging also reported unclassified pixels, without the diagnostic absorptions, which were typically empty vesicles, plagioclase, or certain primary iron oxides.

Finally, a profile of relative mineral abundance vs. depth was obtained for the field data through linear unmixing of the 780 point spectra using averaged endmember pixels from UCIS. A singular value decomposition-based approach was used as described by Boardman (1989) with a unity constraint on endmember abundance, i.e. the constraint that the sum of the abundances of all the endmembers must equal 1. Endmembers are shown in Figure 1, and the results are shown in Figure 4 as "core-stack images", which are further described below. While it is understood that non-linear mixing effects occur in VIS-SWIR spectra of mineral assemblages (Hapke, 1981), we provide these data only as rough abundances for the sake of visualization.

Scanning Electron Microscopy Data Collection

Preparation of the previously analyzed cut sections for SEM-EDS analysis presented many challenges due to the vesicular nature of basalt and its pervasive alteration in some portions of the core. The cut sections were trimmed parallel to a thin-section (dimensions of ~27 x 46 mm) before polishing all eight samples. The samples were polished through a series of grit sizes (from 30µm to 1 µm) with silicon carbide followed by a final polish with diamond paste to ensure a flat surface for sufficient and uniform X-ray count rates for EDS mapping of elemental composition.

Carbon-coated cut sections (~1-2 mm thickness) were examined on a JEOL 6010LA W-filament SEM at the University of Nevada, Reno for textures and morphology at a range of magnifications (~40–7000x). Select areas of samples were mapped by EDS for local elemental composition mapping. Areas were selected to capture the entire range of alteration mineral diversity characterized from the UCIS data. EDS analyses were generally performed at a lower magnification (50x to 190x) and focused on identifying elemental abundances to a few percent relative accuracy within alteration products in order to aid in mineral identification.

X-Ray Diffraction Data Collection

Bulk XRD analyses of 24 samples distributed throughout the core (Table 1) were performed on a Rigaku Smartlab diffractometer at NASA Ames Research Center. Samples were ground with a pestle and mortar to less than 120 µm, before being milled for 5 minutes with ethanol in a McCrone XRD-mill, equipped with zirconium grinding elements. Milled slurries were dried before side-packing the resulting powders into holders. XRD patterns were collected using a scintillation detector with Cu Kα radiation. Patterns were collected between $2^{\circ}<2\theta<65^{\circ}$ 2θ in 0.02º steps, counting for 2 seconds per step. Minerals were identified using Jade MDI software. Relative mineral abundances of clay minerals were estimated from patterns by Rietveld refinement using BGMN software (Bergmann et al., 1998) (Table 1). UCIS-imaged samples were examined on a later date using the same methods. Randomly oriented, and both air dried as well as glycolated oriented preparations of the <0.5 µm fraction (separated by centrifugation) of a subset of sample powders were also measured by the Rigaku Smartlab instrument to characterize phyllosilicate structures (Appendix Figure 4).

Results

Ten spectral endmembers were identified in the UCIS data via the microimaging spectroscopy methods discussed above and cross-checked with SEM and bulk XRD. Four different primary endmembers and six alteration endmembers were found across the eight cut-sections. These endmembers are shown as averages of classified UCIS pixels in Figure 1.

The primary endmembers included two spectrally distinct pyroxenes, olivine, and a mixture of fine-grained primary minerals with iron oxides. The two pyroxenes showed strong, characteristic absorptions near 1 µm, one centered at ~0.99µm and the other at 1.02µm, a 3-channel difference. The endmember with the shorter wavelength absorption ("fine-grained augite") ($(Ca,Na)(Mg,Fe,Al,Ti)(Si,Al)_2O_6$) was more dispersed throughout the samples while the longer wavelength absorption endmember ("coarse-grained augite/diopside") was concentrated in larger crystals and had a well-developed 0.63 µm absorption feature. Both pyroxenes exhibited a strong, broad 2.3-µm absorption. The olivine endmember showed a strong, broad triplet absorption between 1.0-1.25 µm, which varied slightly in shape and was flat through the SWIR after a significant rise in reflectance to 1.80 µm. The "aphanitic matrix material" endmember has a strong absorption in the visible at ~0.55 µm and is flat elsewhere in the spectrum.

The alteration endmembers included three distinct zeolite types, two distinct saponite types, and a possible zeolite-smectite mixture. The "heulandite-phillipsite-like" (Heulandite (Ca): $(Ca,Na)_{2\text{-}3}Al_3(Al,Si)_2Si_{13}O_{36}•12(H_2O)$, Phillipsite: $(Ca,Na_2,K_2)_3Al_6Si_{10}O_{32}\cdot 12H_2O$) zeolites captured the same spectral features as many other zeolites: weak absorptions at 0.97 and 1.16 µm, very strong, moderately broad water absorptions at 1.43 and 1.92 µm, and an overall high albedo with a steep drop-off beyond 2.20 µm. "Analcime" ($NaAlSi_2O_6•(H_2O)$) was nearly identical, but with a characteristic 1.79 µm, medium-strength absorption. The "scolecite-natrolite-like" (Scolecite: $CaAl_2Si_3O_{10}•3(H_2O)$, Natrolite:$Na_2Al_2Si_3O_{10}•2(H_2O)$) endmember had a strong blue slope, with steep, asymmetric absorptions at 1.1, 1.45, and 1.94 µm, in addition to a weak 0.97 µm absorption. The two saponites (low and high-Al saponite) were differentiated by the shape of their 2.32 µm absorption, and the presence/absence of a 2.245 µm absorption feature associated with ferrous Fe and Al. The "zeolite-smectite mixture" was spectrally similar to the "high-Al saponite" endmember but had an exceptionally broad 1.91 µm water feature and elevated reflectance throughout the VNIR, similar to all zeolite endmembers.

Semi-quantitative EDS-derived elemental compositions supported the spectral data and narrowed the possible range of specific mineral species. Table 2 shows EDS-derived elemental compositions for all endmembers and additional primary material. Both pyroxenes contain similar amounts of Fe, Mg, and Ca in general, but showed distinctive differences between the two spectral endmembers. The fine-grained clinopyroxene contains more Al (~4 wt%) and less Ca (~7 wt%) compared to the coarse-grained clinopyroxene. The range of values suggests the finer grained material is augite and the coarser material may be diopside or more Ca-rich augite. EDS data of olivine consistently yield wt% Mg/Fe ratios of ~2-3, demonstrating a forsteritic composition. The "aphanitic matrix material" contains a mixture of fine-grained iron oxides at low abundances with plagioclase/clinopyroxene/ilmenite and very minor amounts of Na.

The saponites are Mg-dominated, and the low-Al phase wt% Mg/Fe ratio ranges from ~1.40-2.0 across all cut-sections, while the higher-Al phase ranges from ~2.1-3.0 and is only measured in SR-459. The zeolite-smectite mixture is chemically similar to the high-Al saponite but has an elevated Si/Al ratio (~4 vs ~3, respectively). The higher Al phase appears to have slightly higher Ca, but the Ca abundances are too low to determine this with confidence. The "heulandite-phillipsite-like" endmember is variable in cation abundance, yielding K or Ca across different cut sections, but has a consistent wt% Si/Al ratio of ~3, which is consistent with either heulandite or phillipsite. Analcime shows very high Na and a wt% Si/Al ratio of >2, whereas scolecite-natrolite contains a mixture of Ca and Na and a wt% Si/Al ratio of <2.

XRD provided verification of saponite as the dominant phyllosilicate throughout the core (based on significant expansion upon glycolation to ~17 Å for all clay fractions and an (060) peak at ~1.53 Å), and also identified heulandite, natrolite, phillipsite, and analcime in several of the cut sections. Hematite was only detected in two samples (SR-537 and -631), while ilmenite was noted in nearly all samples. Olivine was only found at depths shallower than about 1360 m, while plagioclase and pyroxene were noted to persist through the bottom of the zone of analysis. Sparse quartz is noted in two samples towards the bottom of the hole, while sparse orthoclase is identified in only one sample. Table 1 shows XRD identifications and estimated saponite abundances. Figure 5 shows bulk XRD patterns from samples SR-425, -503, -513, and -537. Despite bulk XRD being performed on different pieces of the same samples, the only major discrepancies in identifications are that SR-513 contains weak analcime peaks in XRD, and zeolites noted in SR-618 by UCIS are not seen in XRD. A weak 1.79 μm absorption is present in the interior of pixels classified as natrolite by SFF in sample SR-513 and is also noticeable in the point spectrum of the cut face. The lack of identification of heulandite-phillipsite in SR-618 is likely due to loss during sample preparation, or heterogeneity of the sample. Additional XRD patterns (both bulk and clay fraction) for a subset of samples not examined with UCIS are included in the supplement.

Spatially mapped spectral endmembers can be seen in Figure 3 with a corresponding true-color image in Figure 2. Depths of each of the cut sections discussed below are noted in Table 1.

Mineralogical Variation within Core Samples

SR-392 (1032 m depth), collected closer to the top of the core hole, was devoid of alteration minerals. SR-425 (1125 m depth) represented a transitional zone where fresh olivine was still present, but smectites had formed from olivine crystals preferentially in fractures, as seen in Figure 6. Though both SR-392 and SR-425 are vesicular, empty vesicles are devoid of alteration minerals. This can be observed in Figure 2 in the true color images. All saponite in SR-425 is spatially associated with large crystals of olivine and is low in Al.

SR-459 (1216 m depth) is also representative of phyllosilicate formation and shows the only presence of the zeolite-smectite mixture and the high-Al saponite in the UCIS imaged cut sections. Also co-occurring are coarse-grained augite/diopside and low-Al saponite, but no unmixed zeolites are present.

Both SR-503 (1346 m depth) and SR-513 (1379 m depth) were zeolite dominated, though SR-513 also contained low-Al saponite. In addition to zeolites, pure-silica veinlets were identified via SEM in SR-503. There was a clear replacement process occurring in SR-513 (see Figure 6), with scolecite-natrolite-like endmembers being replaced by a heulandite-phillipsite-like zeolite. SR-537 (1452 m) was dominated by saponite, but had small occurrences of a heulandite-phillipsite-like zeolite. In both SR-503 and SR-537, Fe-rich aphanitic matrix material dominated, and clinopyroxene features were weak.

Alteration in SR-560 (1522 m depth) produced low-Al saponite material. This cut section lacked zeolites, and many of the phyllosilicate occurrences were nearly perfectly spherical (see Figures 2 and 3). In SR-618 (1699 m depth) alteration mineralogy was primarily composed of a fibrous, radiating zeolite with a higher Si/Al ratio. This zeolite may be clinoptilolite or mordenite, but the spectral and EDS data are poor quality due to the sample morphology, making specific identification difficult. Coatings of saponite on vesicles were also present, though not pervasive. XRD identified only saponite on another piece of the same sample.

Alteration in Point Spectra

Through linear unmixing, relative mineral abundances were determined for all 781 field spectra collected from the drill core to determine changes in mineralogy with depth. Zones of zeolite or phyllosilicate dominance were clear, but most of the core contains mixtures as observed in the UCIS imagery. The 2.245-μm, 2.32-μm high-Al saponite was more abundant higher in the stratigraphy. The low-Al saponite was stratigraphically pervasive starting at depths of about 1200 m, generally increasing in abundance with depth. Analcime was present in a few small zones higher in the hole, but was more abundant at intermediate depths through the bottom of the hole. Zeolites were generally present as mixtures at spatial scales below the ~1.5 cm footprint of the point spectrometer (as seen in most of the UCIS images at 240 μm/pixel).

Linear unmixing was accomplished with UCIS scene endmembers. Final RMSE values for the field spectra were a maximum, mean, and standard deviation 0.038, 0.0037, and 0.0028, respectively. It is noted that the higher RMSE values using UCIS endmembers were concentrated in areas of exceptionally sharp featured zeolites. This is likely due to weakened feature strength of the “heulandite-phillipsite-like” target endmember produced from UCIS pixel averaging, where mixing with primary minerals occurs due to its fibrous crystal habit in SR-618.

A three-band composite was formed into an RGB image using summed linear unmixing results to show relative mineral abundances correlated with depth. The three bands chosen were primary (olivine+clinopyroxene+aphanitic matrix material) in red, zeolites (scolecite-natrolite-like + heulandite-like + analcime) in blue, and smectite (high-Al saponite+low-Al saponite) in green. The RGB composite allows for observation of mixtures between the three distinctly different spectral types and demonstrates stratigraphic control of the mineral assemblages better than single matches. Point spectra of the cut face for each slab analyzed with UCIS are shown in Figure 4, color-coded to approximate what the spectrum would look like in the adjacent RGB composite. Figure 4 also shows an alteration "exaggerated" form of the RGB composite, where primary mineral abundances have been artificially reduced by 50% in order to emphasize the alteration colors and distinct zones.

Interpretation

The bulk matrix chemistry and primary mineralogy show a tholeiitic composition, based on the SEM-EDS. This means that all cut sections are likely from shield-stage lava flows, rather than younger alkali-rich post-shield phase lavas. These shield phase lavas are not presently exposed on the surface (Wolfe, Wise, and Dalrymple, 1997) and have not been extensively studied in the past with a focus on alteration. As members of the upper portions of the shield phase, their age is likely ~350-500 ka (Wolfe, Wise, and Dalrymple, 1997). The samples used in this study were collected below the level at which continuous groundwater was encountered during drilling (Jerram et al., 2019), but the discontinuous alteration likely indicates complex lateral and vertical migration of groundwater controlled by physical rock properties and closing of pathways by secondary mineralization.

Sulfates and carbonates are distinctly absent in the cut sections and all field spectra. The lack of Fe^{3+} oxide formation (with the exception of hematite in the matrix material of SR-537, and detection by XRD in SR-631), jarosite-family minerals, kaolinite/illite, and palagonite indicate that alteration occurred at depth in a low-oxygen environment. The saponite clay occurred in vesicles, but primarily as a replacement of olivine. Augite appeared to stay intact and spectrally pristine at depth, though the higher-Ca, coarse-grained pyroxene that was present at shallow depths did not appear at depths and may not have initially been present or may have been replaced. Glass was not identified by any of the analytical methods and is likely completely replaced by saponite or zeolites below the largely unaltered portion of the hole. Primary oxides (ilmenite) remain unaltered through the bottom of the core.

No high-temperature minerals were identified, and the mineralogy is all consistent with the modern geothermal gradient. Heulandite is generally a higher-temperature zeolite but can still form at temperatures as low as 84 °C (Wohletz and Heiken, 1992). Epidote and prehnite, indicative of temperatures of ~250-300 °C (e.g. Freedman et al., 2009) were absent. Viennet et al. (2017) described the preferential formation conditions of phyllosilicates, zeolites, and carbonates in detail. They note that Ca-zeolite formation implies a lack of dioctahedral clay formation, and that under mildly acidic conditions, dioctahedral clay minerals and carbonate minerals are preferentially formed. Trioctahedral clay minerals preferentially formed in conditions with near neutral pH values but can form across a wide range, and zeolites are favored at $pH > 7.2$. Ca-zeolites are present here as both phillipsite and heulandite, which are abundant and present throughout much of the stratigraphy. Because saponite and zeolites often co-occur in this core, it is likely that any stratigraphic control on abundance of zeolites versus smectites is probably caused by availability of olivine or basaltic glass as a source of Mg^{2+} and small pH fluctuations from near neutral to basic.

The scolecite-natrolite-like zeolites were replaced by heulandite-phillipsite-like zeolites at depth in at least one case (see SR-513 in Figure 3 and Figure 6). This could be due to rising temperatures and pressures, or an earlier Na^+ rich fluid being overprinted by a more recent Ca^{2+} rich fluid. Stratigraphic, temperature-controlled zonation like that described by Weisenberger et al. (2009) is not clear in the spectral data for this analyzed section of the core, with all three spectral types persisting from intermediate depths through the bottom of the hole in multiple discontinuous zones. However, bulk XRD results (Table 1) could imply a transition from phillipsite to heulandite at roughly 1460 m, a transition that could be temperature dependent.

EDS values of all smectites analyzed from the cut sections record a wt% Mg/Fe ratio of ~1.5 to slightly over 3, showing magnesium dominance. Trioctahedral Fe/Mg smectites of this composition have a Mg-OH absorption between 2.309 and 2.317 µm (e.g. Michalski et al., 2015), consistent with all distinct smectites observed in all the UCIS cut sections. This feature shifts to shorter wavelengths as oxidation progresses, thus indicating only weak oxidation of these samples (Chemtob et al., 2017). Results show only two samples (537 and 631) with detectable hematite using bulk XRD. Combined with the exclusively trioctahedral phyllosilicate structure observed with both bulk XRD and clay-fraction XRD, most evidence points to Fe^{2+}-rich, trioctahedral smectites with minimal dioctahedral mixing or oxidation. However, variable strength of 0.70, 0.91, and 1.11 µm Fe^{2+} and Fe^{3+} electronic transitions and Fe^{2+}-Fe^{3+} charge-transfer transition features (Chemtob et al., 2017), varying shape of the 2.32 µm feature, particularly on the short-wavelength side (Appendix Figure 3), and iddingsite formation (Calvin et al., in press) hint towards possible dioctahedral mixing and incipient oxidation in some samples. Mössbauer spectroscopy would need to be performed to confirm oxidation states and verify octahedral composition and occupancy.

Interlayering of smectite and chlorite or other phyllosilicates, a process seen elsewhere on Earth and on Mars (Ehlmann and Edwards, 2014), is possible in the case of the high-Al saponite, and the "zeolite-smectite mixture" (which may simply be a more water-saturated form of the high-Al saponite). The abundant Mg^{2+} availability from olivine, the heightened Al levels (Beaufort et al., 1997), and the 2.245 μm absorption feature point to this as a possibility. However, trioctahedral smectites often have an absorption at 2.245 μm from the AlAl(Fe^{2+},Mg)-OH combination band (Chemtob, 2015) as well. Increasing Al levels from Al^{3+} substitution in the octahedral layer are noted to increase the depth of the 2.245 μm feature (Chemtob et al., 2015). Glycolated clay fraction XRD patterns (Appendix Figure 4) show full expansion of (001) spacings to ~17-17.7 Å across the range of spectral variability of the M-OH features seen, with no (002) reflection near 7-7.5 Å indicative of chlorite, and no remnant ~14 Å (001) peak after glycolation. Thus, the heightened Al is likely from a combination of both tetrahedral and octahedral Al^{3+}, and not enough Mg^{2+}/Fe^{2+} substitution by Fe^{3+} or Al^{3+} to lead to a significant dioctahedral character in the XRD patterns. The 2.245 μm feature is more abundant and stronger shallower in the hole, but persists through the bottom. While the spatial segregation of the low-Al and high-Al phases in SR-459 might point to different fluid sources and alteration events, more data are needed to verify whether the 2.245 μm absorption present throughout the hole is only from the high-Al saponite.

Nearly all of the collected data are representative of low to moderate temperature aqueous alteration from moderate to basic pH fluid in low oxygen conditions.

Hydrothermal brines or acidic fluids derived from sulfide weathering likely did not affect these samples.

Implications for Mars Exploration

Smectites and Zeolites on Mars

Fe- and Mg-rich phyllosilicates make up the bulk of aqueous alteration mineralogy that has been identified on the Martian surface via orbital VIS-SWIR spectroscopy (e.g., Carter et al., 2013; Ehlmann and Edwards, 2014). However, the distribution of hydrous phyllosilicate phases raises many questions. Both dioctahedral and trioctahedral smectites have been observed on Mars from orbit and in-situ (e.g., Ehlmann and Edwards, 2014; Vaniman et al., 2014; Bristow et al., 2018), and current oxidation states of Fe provide a snapshot of the outcome of several environmental possibilities during their formation and post-formation history. Trioctahedral, Fe^{2+}-bearing smectites are present on Mars in the lower units of stratigraphic sections exposed by erosion, in materials exhumed by impact, and in diagenetically altered sediments in Gale crater (Bishop et al., 2008; Ehlmann et al., 2011a; Bridges, 2014; Treiman et al., 2014; Vaniman et al., 2014). Trioctahedral, Fe-Mg smectites are the thermodynamically-favored product of lower-temperature, anoxic aqueous alteration of basaltic material (Catalano, 2013). Smectites with an absorption closer to 2.30 μm, which are predominately interpreted as dioctahedral, Fe^{3+}-rich smectites (i.e. nontronite) are the most abundant smectite identified in CRISM pixels (> 70% of smectite identifications) (Michalski et al., 2015). These smectites may have formed from prolonged oxidation of trioctahedral smectites which formed under low-oxygen conditions, or they may have formed directly under oxic aqueous conditions (Chemtob et al., 2015, 2017; Gainey et al., 2017). These varying formation conditions place very different constraints on Mars' atmospheric transitions and regional phenomena. The samples from this study of Mauna Kea drill cores provide an example of trioctahedral smectites formed under low-oxygen conditions, which are generally difficult to study due to their instability on Earth's surface where they are rapidly weathered or oxidized (Chemtob et al., 2017). The co-occurrence of smectite with either primary or associated alteration minerals affects the shape and band position of the Mg-OH feature, which is generally used to identify dioctahedral versus trioctahedral smectite phases. The spectra provided in the supplement here exhibit a range of shapes for trioctahedral smectites of very similar composition (Appendix Figure 2), but mixed with different mineralogy based on their stratigraphic occurrence. Additionally, the ~2.25 μm feature commonly used in remote sensing studies to identify chlorite is shown here to be present and strong in naturally occurring saponite with likely no chlorite component in Mars-like lithology.

Zeolites are both a possible component of the widespread dust on Mars and an aqueous alteration product, much like on Earth where they replace glassy material and infill amygdaloidal cavities of volcanic rocks and volcaniclastic sediment (Ruff, 2004; Ehlmann et al., 2009; Ehlmann and Edwards, 2014; Viennet et al., 2017). Though many of the zeolite species are spectrally similar, their presence alone in low to moderate temperature aqueous alteration of basalt and basaltic glass provides limits on pH (Viennet et al., 2017). Analcime, a Na zeolite, has been observed in theorized impact excavated or hydrothermal-generated material on Mars in multiple locations (Ehlmann et al., 2009; Carrozzo et al., 2017). Here we identify analcime and other zeolites and observe how they spectrally mix with smectites and primary mafic minerals. While identifying zeolites in mixtures with hydrated smectites is difficult, mapping of zeolites on Mars has great implications for understanding pH in the early surface and subsurface environment.

Wordsworth et al. (2018) suggest that the characterization of "climatically important mineral deposits" is an important goal for future missions. Spectral characterization of geologically realistic mixtures of Mars-relevant primary and zeolite mineralogy with trioctahedral smectites presents a pathway for identifying this subsurface environment of formation on Mars. In addition, we identify specific features to help differentiate these materials. Further work to better constrain alteration conditions and stratigraphic constraints in these samples, including complete core VIS-SWIR scanning, will provide additional insight into similar environments that were likely present on early Mars.

Acknowledgements

This project was funded in part by the Honors Undergraduate Research Program at the University of Nevada, Reno and by the NASA Solar Systems Workings program Award #80NSSC19K0031 to W.M. Calvin. A portion of this research was carried out at the Jet Propulsion Laboratory, California Institute of Technology, under a contract with the National Aeronautics and Space Administration. We appreciate detailed reviews by Elizabeth Rampe and one anonymous reviewer who helped clarify and strengthen the manuscript.

References Cited

Arvidson, R.E., Bellutta, P., Calef, F., Fraeman, A.A., Garvin, J.B., Gasnault, O., . . . Wiens, R.C. (2014). Terrain physical properties derived from orbital data and the first 360 sols of Mars science laboratory curiosity rover observations in gale crater. Journal of Geophysical Research: Planets, 119(6), 1322-1344.doi:10.1002/2013JE004605

Beaufort, D., Baronnet, A., Lanson, B., & Meunier, A. (1997). Corrensite; a single phase or a mixed-layer phyllosilicate in saponite-to-chlorite conversion series? A case study of Sancerre-Couy deep drill hole (France). American Mineralogist, 82(1-2), 109-124.

Bergmann, J., Friedel, P. & Kleeberg, R. (1998). BGMN — a new fundamental parameters based Rietveld program for laboratory X-ray sources, it's use in quantitative analysis and structure investigations. Commission of Powder Diffraction Newsletter, 20, 5–8

Bibring, J.P., Langevin, Y., Mustard, J.F., Poulet, F., Arvidson, R., Gendrin, A., … Neukum, G. (2006). Global mineralogical and aqueous Mars history derived from OMEGA/Mars Express data. Science, 312(5772), 400–404.

Bishop J.L. and Murad E. (2002) Spectroscopic and Geochemical Analyses of Ferrihydrite from Hydrothermal Springs in Iceland and Applications to Mars. In Volcano-Ice Interactions on Earth and Mars. Geological Society, Special Pub. (202), 357-370.

Bishop, J.L., Dobrea, E. Z.N., McKeown, N.K., Parente, M., Ehlmann, B.L., Michalski, J.R., … Bibring, J.P. (2008). Phyllosilicate diversity and past aqueous activity revealed at Mawrth Vallis, Mars. Science, 321(5890), 830–833.

Bridges, J. (2014). Comparing clays from Mars and Earth: Implications for martian habitability. American Mineralogist. https://doi.org/10.2138/am-2014-5089

Bristow, T.F., Rampe, E.B., Achilles, C.N., Blake, D.F., Chipera, S.J., Craig, P., … Yen, A.S. (2018). Clay mineral diversity and abundance in sedimentary rocks of Gale crater, Mars. Science Advances, 4(6).

Boardman, J.W. (1989). Inversion of imaging spectrometry data using singular value decomposition.

Proceedings, IGARSS'89, 12th Canadian Symposium on Remote Sensing, 4, 2069-2072. 10.1109/IGARSS.1989.577779

Calvin, W.M., and Pace, E.L. (2016). Mapping alteration in geothermal drill core using a field portable spectroradiometer. Geothermics. https://doi.org/10.1016/j.geothermics.2016.01.005

Calvin, W.M., Lautze, N., Moore, J., Thomas, D., Haskins, E., Rasmussen, B.P. (2020). Petrographic and Spectral Study of Hydrothermal Mineralization in Drill Core from Hawaii: A potential analogue to alteration in the Martian subsurface. American Mineralogist, in press.

Campbell, N.A. (1996). The decorrelation stretch transformation. International Journal of Remote Sensing. 17(10), 1939-1949. https://doi.org/10.1080/01431169608948749

Cannon, K.M., Parman, S.W., Mustard, J.F. (2017) Primordial clays on Mars formed beneath a steam or supercritical atmosphere. Nature, doi:10.1038/nature24657

Carrozzo, F.G., Di Achille, G., Salese, F., Altieri, F., and Bellucci, G. (2017). Geology and mineralogy of the Auki Crater, Tyrrhena Terra, Mars: A possible post impact-induced hydrothermal system. Icarus. https://doi.org/10.1016/j.icarus.2016.09.001

Carter, J.,F. Poulet, J.P. Bibring, N. Mangold, and S. Murchie (2013), Hydrous minerals on Mars as seen by the CRISM and OMEGA imaging spectrometers: Updated global view, J. Geophys. Res. Planets, 118, doi: 10.1029/2012JE004145.

Catalano, J. G. (2013). Thermodynamic and mass balance constraints on iron-bearing phyllosilicate formation and alteration pathways on early Mars. Journal of Geophysical Research: Planets. https://doi.org/10.1002/jgre.20161

Clark, R.N., King, T.V., Klejwa, M., Swayze, G.A., & Vergo, N. (1990). High spectral resolution reflectance spectroscopy of minerals. Journal of Geophysical Research: Solid Earth, 95(B8), 12653-12680.

Clark, R.N., Swayze, G.A., Gallagher, A., Gorelick, N., & Kruse, F.A. (1991). Mapping with imaging spectrometer data using the complete band shape least-squares algorithm simultaneously fit to multiple spectral features from multiple materials. Proceedings of the third airborne visible/infrared imaging spectrometer (AVIRIS) workshop 42, 2-3

Chemtob, S.M., Nickerson, R.D., Morris, R.V., Agresti, D.G., and Catalano, J.G. (2015). Synthesis and structural characterization of ferrous trioctahedral smectites: Implications for clay mineral genesis and detectability on Mars. Journal of Geophysical Research: Planets. https://doi.org/10.1002/2014je004763

Chemtob, S.M., Nickerson, R.D., Morris, R.V., Agresti, D.G., and Catalano, J.G. (2017). Oxidative Alteration of Ferrous Smectites and Implications for the Redox Evolution of Early Mars. Journal of Geophysical Research: Planets. https://doi.org/10.1002/2017je005331

Ehlmann, B.L., and Edwards, C.S. (2014). Mineralogy of the Martian Surface. Annual Review of Earth and Planetary Sciences. https://doi.org/10.1146/annurev-earth-060313-055024

Ehlmann, B.L., Bish, D.L., Ruff, S.W., and Mustard, J.F. (2012). Mineralogy and chemistry of altered Icelandic basalts: Application to clay mineral detection and understanding aqueous environments on Mars. Journal of Geophysical Research: Planets. https://doi.org/10.1029/2012je004156

Ehlmann, B.L., J.F. Mustard, S.L. Murchie, J.P. Bibring, A. Meunier, A.A. Fraeman, and Y. Langevin (2011a), Subsurface water and clay mineral formation during the early history of Mars, Nature, 479, 53–60, doi:10.1038/nature10582.

Ehlmann, B.L., J.F. Mustard, R.N. Clark, G.A. Swayze, and S.L. Murchie (2011b), Evidence of low-grade metamorphism, hydrothermal alteration, and diagenesis on Mars from phyllosilicate mineral assemblages, Clays and Clay Minerals., 59(4), 359–377.

Ehlmann, B.L., Mustard, J.F., Swayze, G.A., Clark, R.N., Bishop, J.L., Poulet, F., … Murchie, S. L. (2009). Identification of hydrated silicate minerals on Mars using MRO-CRISM: Geologic context near Nili Fossae and implications for aqueous alteration. Journal of Geophysical Research. https://doi.org/10.1029/2009je003339

Freedman, A.J., Bird, D. K., Arnórsson, S., Fridriksson, T., Elders, W.A., & Fridleifsson, G.Ó. (2009). Hydrothermal minerals record CO2 partial pressures in the Reykjanes geothermal system, Iceland. American Journal of Science, 309(9), 788-833.

Gainey, S.R., Hausrath, E.M., Adcock, C.T., Tschauner, O., Hurowitz, J.A., Ehlmann, B.L., . . . (2017). Clay mineral formation under oxidized conditions and implications for paleoenvironments and organic preservation on mars. Nature Communications, 8(1), 1230-7. doi:10.1038/s41467-017-01235-7

Greenberger, R.N., Mustard, J.F., Ehlmann, B.L., Blaney, D.L., Cloutis, E.A., Wilson, J.H., … Fraeman, A.A. (2015). Imaging spectroscopy of geological samples and outcrops: Novel insights from microns to meters. GSA Today. https://doi.org/10.1130/gsatg252a.1

Grotzinger, J.P.,Sumner, D.Y., Kah, L. C., Stack, K.,Gupta, S., Edgar, L., ... & Milliken, R. (2014). A habitable fluvio-lacustrine environment at Yellowknife Bay, Gale Crater, Mars. Science, 343(6169),1242777.

Greenberger, R.N., Mustard, J.F., Kumar, P.S., Dyar, M.D., Breves, E.A., and Sklute, E.C. (2012). Low temperature aqueous alteration of basalt: Mineral assemblages of Deccan basalts and implications for Mars. Journal of Geophysical Research: Planets. https://doi.org/10.1029/2012je004127

Guinness, E.A., Arvidson, R.E., Jolliff, B.L., Seelos, K.D., Seelos, F. P., Ming, D.W., … Graff, T.G. (2007). Hyperspectral reflectance mapping of cinder cones at the summit of Mauna Kea and implications for equivalent observations on Mars. Journal of Geophysical Research: Planets. https://doi.org/10.1029/2006je002822

Hadnott, B.A., Ehlmann, B.L., and Jolliff, B.L. (2017). Mineralogy and chemistry of San Carlos High-Alkali basalts: Analyses of alteration with application for Mars exploration. American Mineralogist. https://doi.org/10.2138/am-2017-5608

Hapke, B (1981). Bidirectional reflectance spectroscopy: 1. Theory. Journal of Geophysical Research: Solid Earth 86, 3039-3054.

Hunt, G.R. (1977). Spectral signatures of particulate minerals in the visible and near infrared. Geophysics, 42, 501-513.https://doi.org/10.1190/1.1440721

Jerram, D.A., Millett, J.M., Kück, J., Thomas, D., Planke, S., Haskins, E., Lautze, N., and Pierdominici, S. (2019) Understanding volcanic facies in the subsurface: a combined core, wireline logging and image log data set from the PTA2 and KMA1 boreholes, Big Island, Hawai`i. Scientific Drilling, 25, 15-33.

King, T.V.V., and Clark, R.N. (1989). Spectral characteristics of chlorites and Mg-serpentines using high-resolution reflectance spectroscopy. Journal of Geophysical Research: Solid Earth. https://doi.org/10.1029/jb094ib10p13997

Kokaly, R.F., Clark, R.N., Swayze, G.A., Eric Livo, K., Hoefen, T.M., Pearson, N. C., … Klein, A.J. (2017). USGS Spectral Library Version 7. Data Series. https://doi.org/10.3133/ds1035

Leask, E.K., and Ehlmann, B.L. (2016). Identifying and quantifying mineral abundance through VSWIR microimaging spectroscopy: A comparison to XRD and SEM. 2016 8th Workshop on Hyperspectral Image and Signal Processing: Evolution in Remote Sensing (WHISPERS). https://doi.org/10.1109/whispers.2016.8071774

McCanta, M.C., Dyar, M.D., and Treiman, A.H. (2014). Alteration of Hawaiian basalts under sulfur-rich conditions: Applications to understanding surface-atmosphere interactions on Mars and Venus. American Mineralogist. https://doi.org/10.2138/am.2014.4584

Michalski, J.R., Cuadros, J., Bishop, J.L., Darby Dyar, M., Dekov, V., and Fiore, S. (2015). Constraints on the crystal-chemistry of Fe/Mg-rich smectitic clays on Mars and links to global alteration trends. Earth and Planetary Science Letters. https://doi.org/10.1016/j.epsl.2015.06.020

Michalski, J.R., Cuadros, J., Niles, P.B., Parnell, J., Deanne Rogers, A., and Wright, S.P. (2013). Groundwater activity on Mars and implications for a deep biosphere. Nature Geoscience. https://doi.org/10.1038/ngeo1706

Morris, R.V., Gooding, J.L., Lauer, H.V., & Singer, R.B. (1990). Origins of Marslike spectral and magnetic properties of a Hawaiian palagonitic soil. Journal of Geophysical Research: Solid Earth, 95(B9), 14427-14434.

Morris, R.V., Ming, D.W., Graff, T.G., Arvidson, R.E., Bell, J.F., Squyres, S.W., … Robinson, G.A. (2005). Hematite spherules in basaltic tephra altered under aqueous, acid-sulfate conditions on Mauna Kea volcano, Hawaii: Possible clues for the occurrence of hematite-rich spherules in the Burns formation at Meridiani Planum, Mars. Earth and Planetary Science Letters. https://doi.org/10.1016/j.epsl.2005.09.044

Morris, R.V., Ruff, S.W., Gellert, R., Ming, D.W., Arvidson, R.E., Clark, B.C., . . . Squyres, S.W. (2010). Identification of carbonate-rich outcrops on Mars by the spirit rover. Science, 329(5990), 421-

424. doi:10.1126/science.1189667

Murchie, S., Arvidson, R., Bedini, P., Beisser, K., Bibring, J. P., Bishop, J., ... & Darlington, E. H. (2007). Compact reconnaissance imaging spectrometer for Mars (CRISM) on Mars reconnaissance orbiter (MRO). Journal of Geophysical Research: Planets, 112(E5).

Pan, L., and Ehlmann, B.L. (2014). Phyllosilicate and hydrated silica detections in the knobby terrains of Acidalia Planitia, northern plains, Mars. Geophysical Research Letters. https://doi.org/10.1002/2014gl059423

Rampe, E. B., Ming, D. W., Blake, D. F., Bristow, T. F., Chipera, S. J., Grotzinger, J. P., Morris, R. V., Morrison, S. M., Vaniman, D. T., Yen, A. S., Achilles, C. N., Craig, P. I., Des Marais, D. J., Downs, R. T., Farmer, J. D., Fendrich, K. V., Gellert, R., Morookian, J. M., Peretyazhko, T. S., Sarrazin, P., Treiman, A. H., Berger, J. A., Eigenbrode, J. L., Fairén, A. G., Forni, O., Gupta, S., Hurowitz, J. A., Kah, L. C., Lanza, N. L., Schmidt, M. E., Siebach, K., Sutter, B., and Thompson, L. M. (2017) Mineralogy of an ancient lacustrine mudstone succession from the Murray formation, Gale crater, Mars. Earth and Planetary Science Letters, 471, 172-185.

Ruff, S.W. (2004). Spectral evidence for zeolite in the dust on Mars. Icarus. https://doi.org/10.1016/j.icarus.2003.11.003

Tornabene, L.L., Osinski, G.R., McEwen, A.S., Wray, J.J., Craig, M.A., Sapers, H.M., and Christensen, P.R. (2013). An impact origin for hydrated silicates on Mars: A synthesis. Journal of Geophysical Research: Planets. https://doi.org/10.1002/jgre.20082

Treiman, A.H., Morris, R.V., Agresti, D.G., Graff, T.G., Achilles, C.N., Rampe, E.B., … Downs, R.T. (2014). Ferrian saponite from the Santa Monica Mountains (California, U.S.A., Earth): Characterization as an analog for clay minerals on Mars with application to Yellowknife Bay in Gale Crater. American Mineralogist. https://doi.org/10.2138/am-2014-4763

Vaniman, D.T., D.L. Bish, D.W. Ming, T.F. Bristow, R.V. Morris, D.F. Blake, S.J. Chipera, S.M. Morrison, A.H. Treiman, E.B. Rampe, M. Rice, C.N. Achilles, J. Grotzinger, S.M. McLennan, J. Williams, J. Bell III, H. Newsom, R.T. Downs, S. Maurice, P. Sarrazin, A.S. Yen, J.M.

Morookian, J.D. Farmer, K. Stack, R.E. Milliken, B.L. Ehlmann, D.Y. Sumner, G. Berger, J.A. Crisp, J.A. Hurowitz, R. Anderson, D. DesMarais, E.M. Stolper, K S. Edgett, S. Gupta, N. Spanovich, MSL Science Team. (2014). Mineralogy of a mudstone at Yellowknife Bay, Gale crater, Mars. Science 343, 1243480. doi:10.1126/science.1243480

Van Gorp, B., Mouroulis, P., Blaney, D., Green, R.O., Ehlmann, B.L., and Rodriguez, J.I. (2014). Ultra-compact imaging spectrometer for remote,in situ, and microscopic planetary mineralogy. Journal of Applied Remote Sensing. https://doi.org/10.1117/1.jrs.8.084988

Viennet, J.C., Bultel, B., Riu, L., and Werner, S.C. (2017). Dioctahedral Phyllosilicates Versus Zeolites and Carbonates Versus Zeolites Competitions as Constraints to Understanding Early Mars Alteration Conditions. Journal of Geophysical Research: Planets. https://doi.org/10.1002/2017je005343

Viviano-Beck, C. E., Seelos, F. P., Murchie, S. L., Kahn, E. G., Seelos, K. D., Taylor, H. W., Taylor, K. Ehlmann, B. L., Wiseman, S. M., Mustard J. F., M. F. Morgan (2014). Revised CRISM spectral parameters and summary products based on the currently detected mineral diversity on Mars, Journal of Geophysical Research: Planets, 119, 1403–1431.

Weisenberger, T and Selbekk, R.S. (2009). Multi-stage zeolite facies mineralization in the Hvalfjördur area. Iceland. International Journal of Earth Science 98. 985-999. 10.1007/s00531-007-0296-6.

Wohletz, K., & Heiken, G. (1992). Volcanology and geothermal energy. Berkeley: University of California Press.

Wolfe, E.W., Wise, W.S., and Brent Dalrymple, G. (1997). The geology and petrology of Mauna Kea Volcano, Hawaii;a study of postshield volcanism. Professional Paper. https://doi.org/10.3133/pp1557

Wordsworth, R., Ehlmann, B.L., Forget, F., Haberle, R., Head, J., and Kerber, L. (2018). Healthy debate on early Mars. Nature Geoscience. https://doi.org/10.1038/s41561-018-0267-5

Figure and Table Captions

Table 1: Phases identified by XRD of all cut sections analyzed in this study. Abundances of trioctahedral clay minerals (saponite) were determined by XRD analyses with the BGMN software (2:1 clay row). UCIS imaged cut-sections have their rows highlighted.

Table 2: Normalized, non-standardized EDS-derived compositions (in mass %) of all spectral endmembers in addition to a bulk average of both distinct matrix materials. All

reported compositions are means of multiple mapped areas, and should be interpreted only in a semi-quantitative sense.

Figure 1: Spectral endmembers produced from in-scene averages of UCIS reflectance pixels. Vertical lines highlight features at 1, 1.2, 1.4, 1.79, 1.91, 2.245, 2.29, 2.32, and 2.4 µm.USGS spectral library standards are included for comparison to UCIS spectra.

Figure 2: True color mosaic of the individual cut section images produced from UCIS images.

Figure 3: Classified image results from spectral feature fitting of in-scene endmembers. Unclassified pixels are generally vesicles, plagioclase grains, or very low signal, low albedo areas. See Appendix Figure 1 for quantification of pixel classes for each sample.

Figure 4: The left spectral stack plot illustrates the point spectra of the cut face of UCIS imaged sections. Vertical lines highlight features at 1, 1.2, 1.4, 1.79, 1.91, 2.245, 2.29, 2.32, and 2.4 µm (also denoted in Figure 1). Line colors in the spectra plots represent approximate colors of spectra in the corresponding “core stack” image to the right. In the vertical color images, the color of a particular location is based on UCIS endmember abundance. Here, relative abundances produced from linear spectral unmixing form red “primary endmembers,” green “saponite endmembers,” and blue “zeolite endmembers” channels in the “raw” image. The second image represents an “alteration exaggerated” form of the RGB composite to the left, where primary mineral abundances have been artificially reduced by 50% in order to emphasize the alteration colors. This better

illustrates to the human eye the stratigraphic pervasiveness of the saponite, and the zeolite zonation. Horizontal black bars represent local zeolite enrichments.

Figure 5: XRD patterns for samples SR-425, -503, -513, and -537, with characteristic peaks annotated.

Figure 6: SEM images demonstrate textural relationships of primary and secondary phases in cut sections. In A, exposed heulandite-phillipsite crystals radiate towards matrix material (SR-503). In B, scolecite-natrolite (interior) is being replaced by heulandite-phillipsite (SR-513). In C, well-organized saponite platelets are exposed by a scratch, and smectite swelling is observed within the high-Al saponite endmember (SR-459). In D, a different texture of heulandite-phillipsite in more tabular crystals is exhibited (SR-503). In E, euhedral olivine crystals are replaced by the low-Al saponite endmember, which is preferentially forming in fractures (SR-425). In F, a radiating zeolite shows a distinctly different texture from the other heulandite-phillipsite occurrences, possibly hinting at a different zeolite phase (SR-618).

Appendix Figure Captions

Appendix Figure 1: Spectral endmember classified pixel abundances from UCIS image mosaic. Unclassified pixels are generally plagioclase and primary oxide grains, though voids in the interior of samples are included in this case.

Appendix Figure 2: Ratioed CRISM Minerals Identified through CRISM Analysis (MICA) spectra (Viviano-beck et al., 2014) of relevant mineralogy compared to both mean UCIS pixels of each sample, and bulk point spectra of each sample.

Appendix Figure 3: Feature shape variation of all UCIS pixels classified as saponite-containing. The ratio values on each axis are of continuum-removed spectra.

Appendix Figure 4: Clay fraction and bulk XRD results for samples SR-446, -541, -544, and -639 and their cut face point spectra for comparison. Each panel shows the 0-35 2θ range both glycolated and air dried, with a zoomed in view of the 59-65 °2θ range. All samples, despite varying VIS-SWIR spectral shapes, are characteristic of saponite.

Tables

Table 1

Pyroxene	Plagioclase
x	x
x	x
x	x
x	x
x	x
x	x
x	x
x	x
x	x
x	x
x	
x	x
x	x
x	x
x	x
x	x
x	x
x	x
x	x
x	x
x	x
x	x
x	x
x	x

Depth (m)	Sample	Quartz	Ilmenite	Hematite	Natrolite	Analcime	Heulandite	Phillipsite	2:1 clay (%)	Olivine
977	373			o						
1032	392		x							x
1119	422		x						30	x
1125	425		x	o					5	x
1153	437		x						10	x
1177	446		x	o					30	
1216	459								30	
1235	465		x						10	
1274	479		x						40	
1346	503		x			x	x		5-10	
1354	505							x	30	x
1379	513		x		x	x		x	35	
1452	537		x	x					15	
1463	541		x					x	50	
1472	544		x							
1521	560		x						10	
1562	573		x						10	
1567	575		x			x			30	
1680	612		x						10	
1685	614		x						5	
1699	618		x						5-10	
1721	626	x	x						25	
1736	631	x		x					10	
1761	639		x						50	

Table 2

Endmember	Fe	Mg	Al	Ca	K	Na	Ti	Si	O	Si/Al	Mg/Fe
Coarse Matrix	6	8.8	4	9.5	0	0	0.8	24.2	46.6	6	1.5
Aphanitic Matrix	16.1	7.4	3.6	8.1	0	0	1.6	19.9	43.4	5.5	0.5
Olivine	10.2	28.5	0	0	0	0	0	18.8	42.85	N/A	2.8

Fine-Grained Clinopyroxene	7.7	7.9	6.5	5.7	0	0.7	0	23.6	47.9	3.9	1
Coarse-Grained Clinopyroxene	6.2	9.4	2.5	13.4	0	0	0	24.9	43.1	12.1	1.5
High-Al Saponite	5	13.4	7.9	2.2	0	0	0	23	48.5	2.9	2.7
Low-Al Saponite	8.7	14.4	3	0.6	0	0	0	25.8	47.5	8.5	1.7
Saponite-Zeolite Mix	5.1	14.2	6.3	2.7	0	0	0	22.8	48.9	3.8	2.8
Heulandite-Phillipsite-Like	0	0.6	10.2	4.6	1.7	1.5	0	26.6	54.8	2.6	N/A
Analcime	0	0	10.8	0	0	11.5	0	26	51.8	2.4	N/A
Scolecite-Natrolite-Like	0	0	14.2	8	0	4.6	0	21.5	51.8	1.51	N/A

Figures

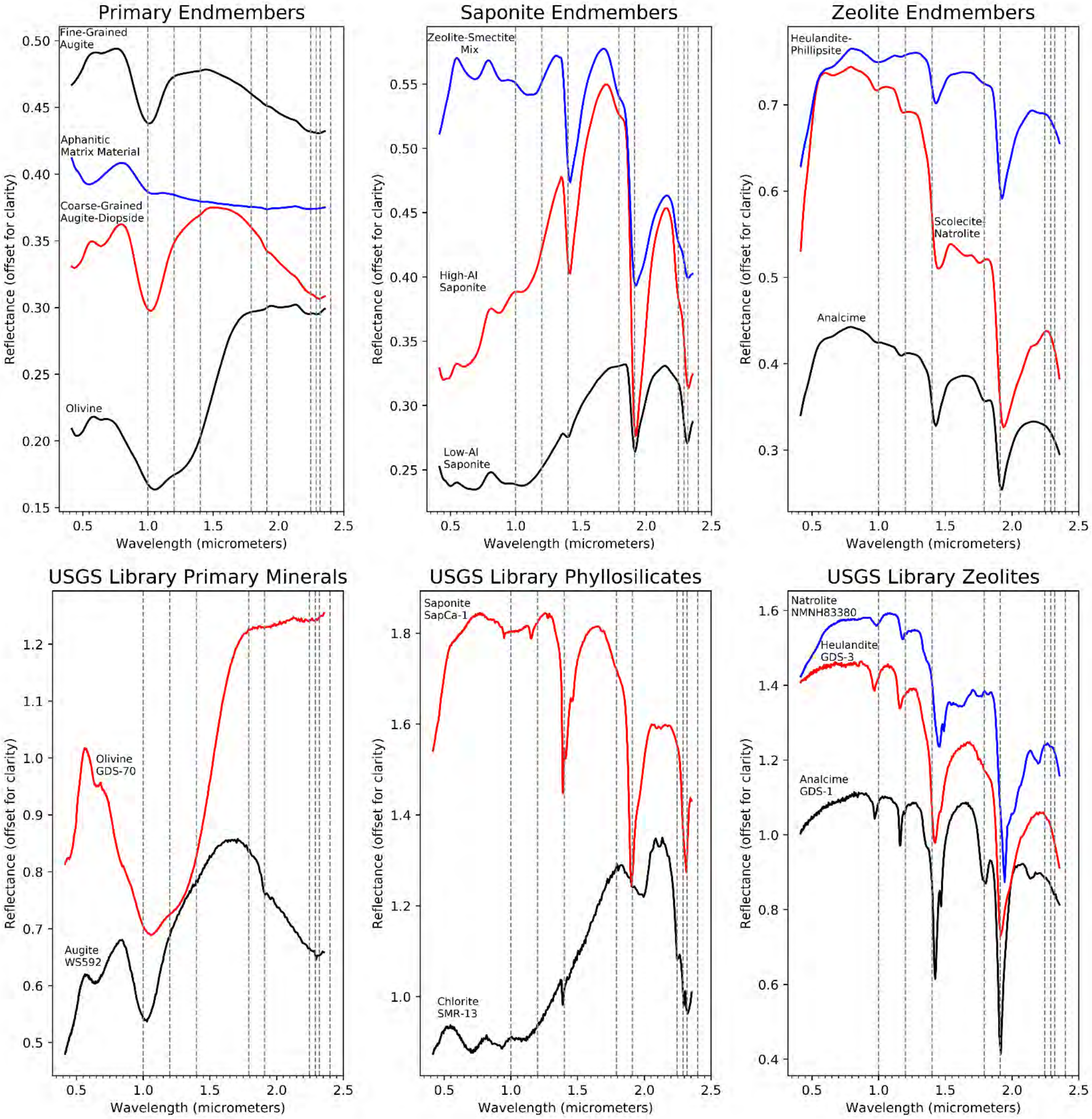

Figure 1

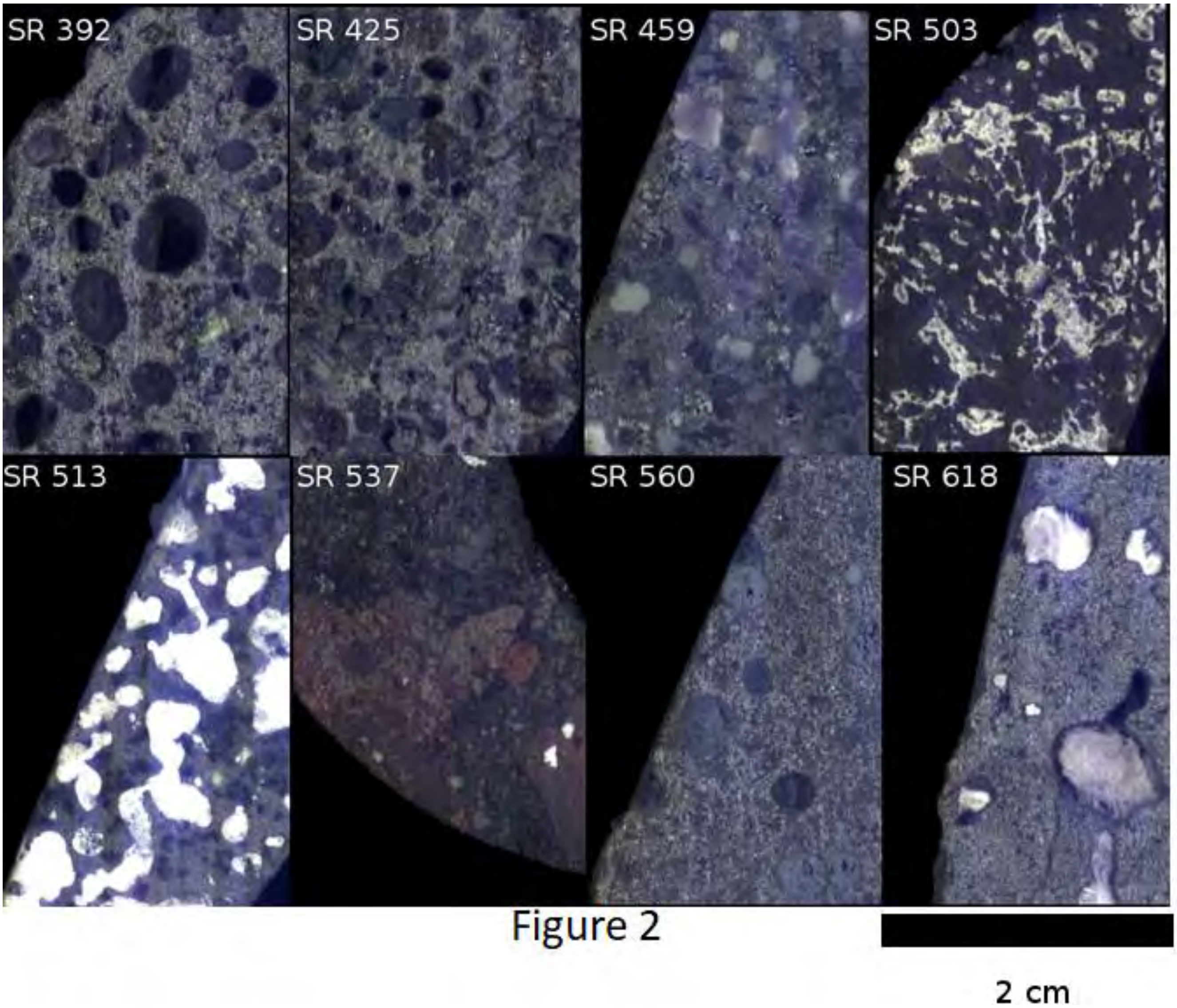

Figure 2

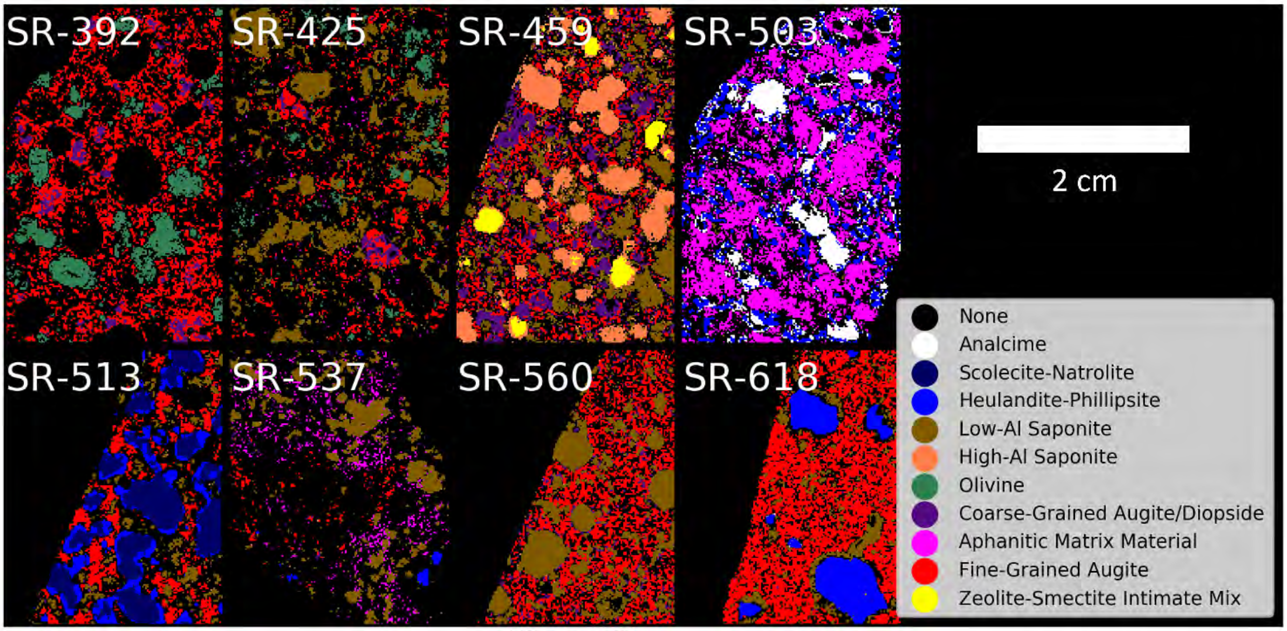
SR-392
SR-425
SR-459
SR-503
2 cm
SR-513
SR-537
SR-560
SR-618
None
Analcime
Scolecite-Natrolite
Heulandite-Phillipsite
Low-Al Saponite
High-Al Saponite
Olivine
Coarse-Grained Augite/Diopside
Aphanitic Matrix Material
Fine-Grained Augite
Zeolite-Smectite Intimate Mix

Figure 3

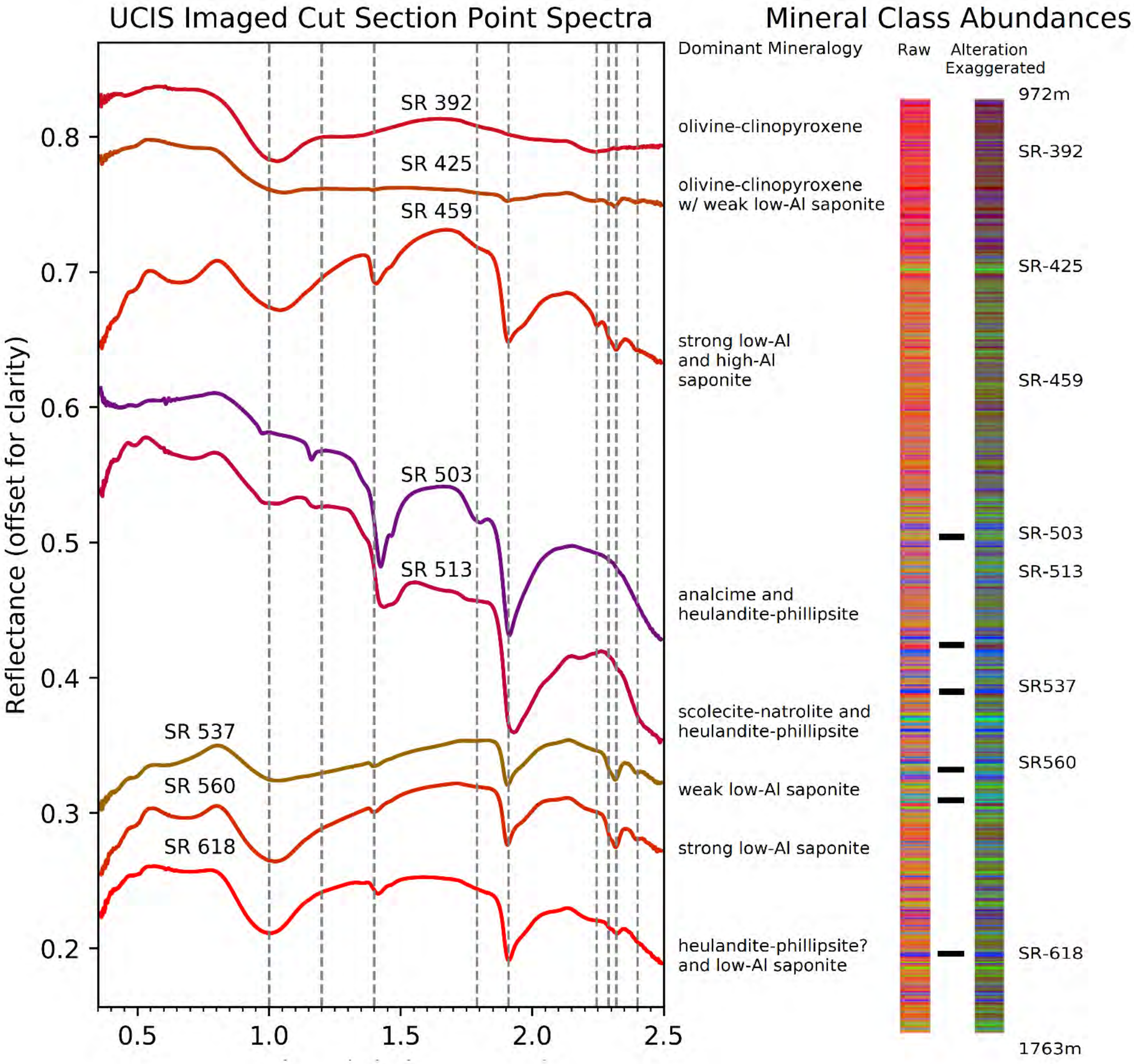
UCIS Imaged Cut Section Point Spectra
Mineral Class Abundances
Reflectance (offset for clarity)
0.8
0.7
0.6
0.5
0.4
0.3
0.2
0.5
1.0
1.5
2.0
2.5
SR 392
SR 425
SR 459
SR 503
SR 513
SR 537
SR 560
SR 618
Dominant Mineralogy
olivine-clinopyroxene
olivine-clinopyroxene w/ weak low-Al saponite
strong low-Al and high-Al saponite
analcime and heulandite-phillipsite
scolecite-natrolite and heulandite-phillipsite
weak low-Al saponite
strong low-Al saponite
heulandite-phillipsite? and low-Al saponite
Raw
Alteration Exaggerated
972m
SR-392
SR-425
SR-459
SR-503
SR-513
SR537
SR560
SR-618
1763m

Figure 4

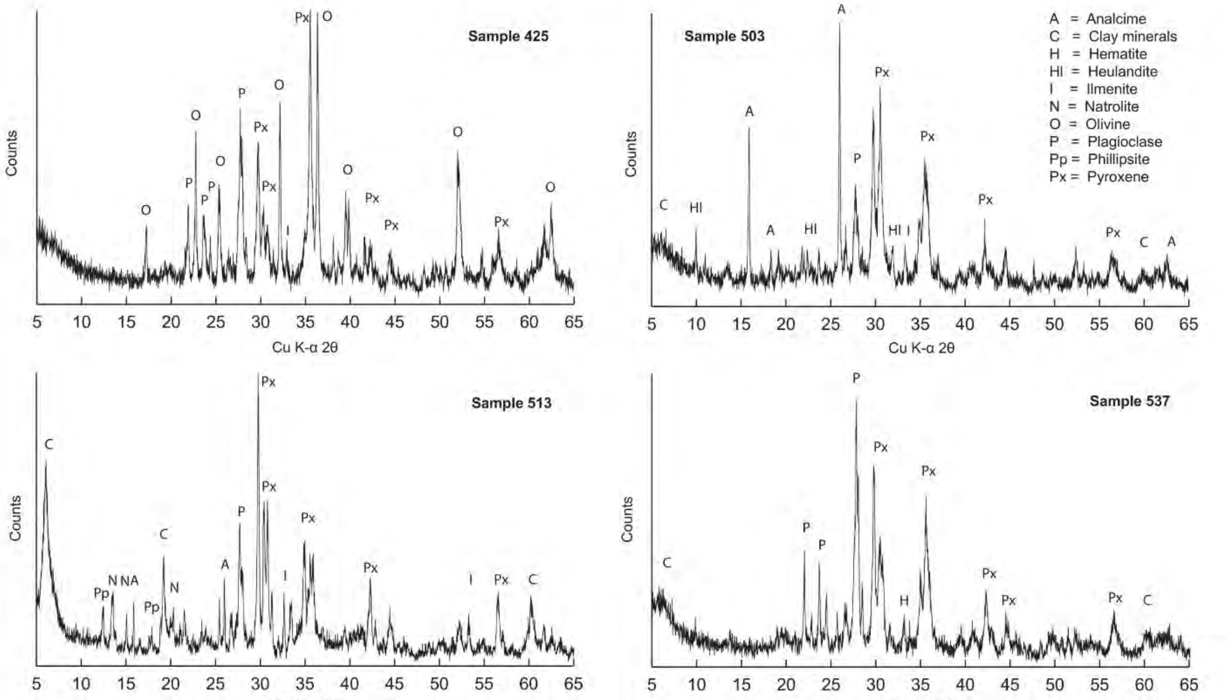
Sample 425
Counts
Cu K-α 2θ
5 10 15 20 25 30 35 40 45 50 55 60 65
O P P O P P O P Px Px O Px O O Px Px Px O O
Sample 503
Counts
Cu K-α 2θ
C Hl A A Hl A P Px Hl I Px Px Px C A
A = Analcime
C = Clay minerals
H = Hematite
Hl = Heulandite
I = Ilmenite
N = Natrolite
O = Olivine
P = Plagioclase
Pp = Phillipsite
Px = Pyroxene
Sample 513
Counts
Cu K-α 2θ
C Pp N NA Pp C N A P Px Px I Px Px I Px C
Sample 537
Counts
Cu K-α 2θ
C P P P Px H Px Px Px Px C

Figure 5

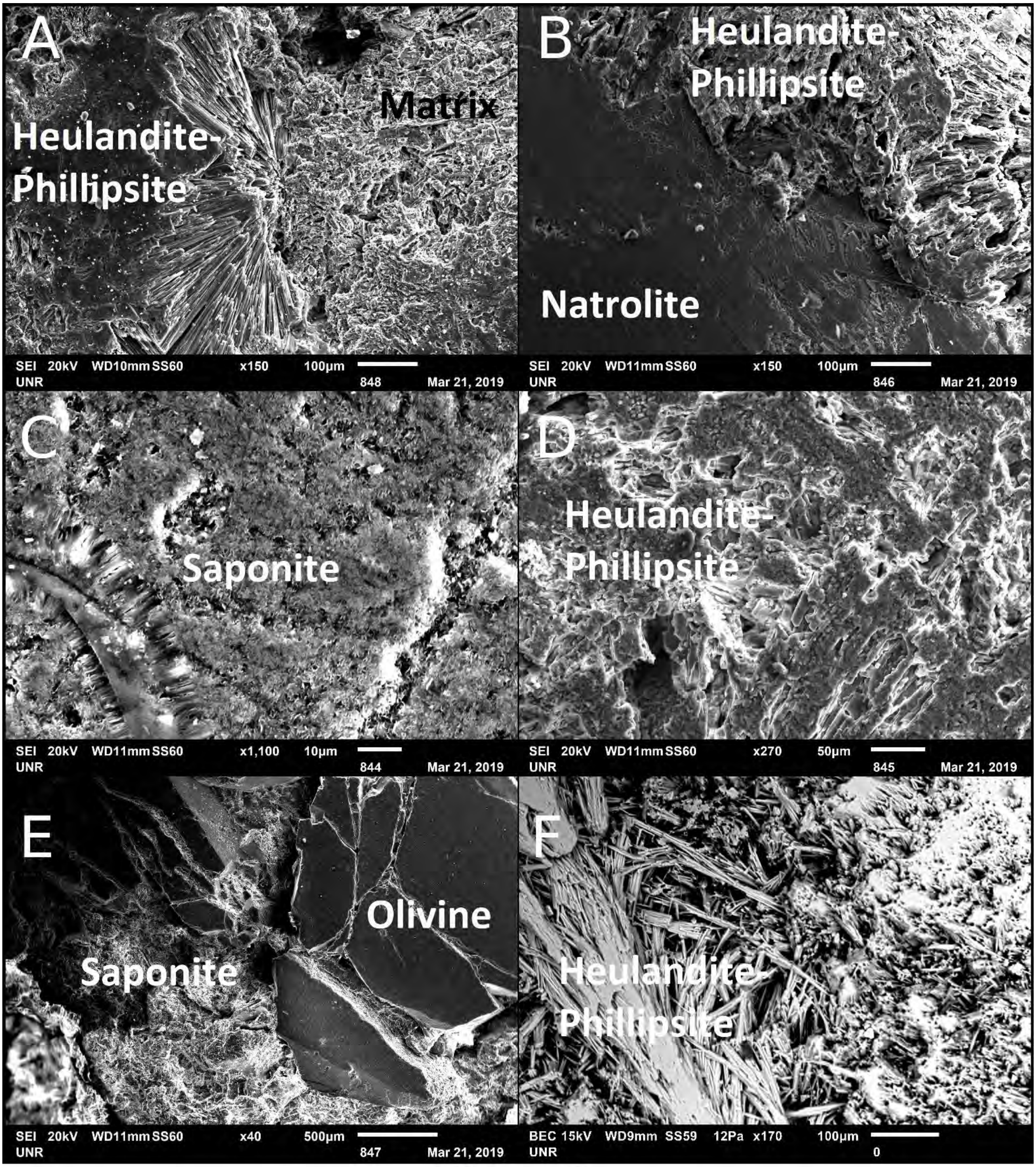
A
Heulandite-Phillipsite
Matrix
SEI 20kV WD10mm SS60 x150 100µm
UNR 848 Mar 21, 2019
B
Heulandite-Phillipsite
Natrolite
SEI 20kV WD11mm SS60 x150 100µm
UNR 846 Mar 21, 2019
C
Saponite
SEI 20kV WD11mm SS60 x1,100 10µm
UNR 844 Mar 21, 2019
D
Heulandite-Phillipsite
SEI 20kV WD11mm SS60 x270 50µm
UNR 845 Mar 21, 2019
E
Olivine
Saponite
SEI 20kV WD11mm SS60 x40 500µm
UNR 847 Mar 21, 2019
F
Heulandite-Phillipsite
BEC 15kV WD9mm SS59 12Pa x170 100µm
UNR 0

Figure 6

Appendix Figures

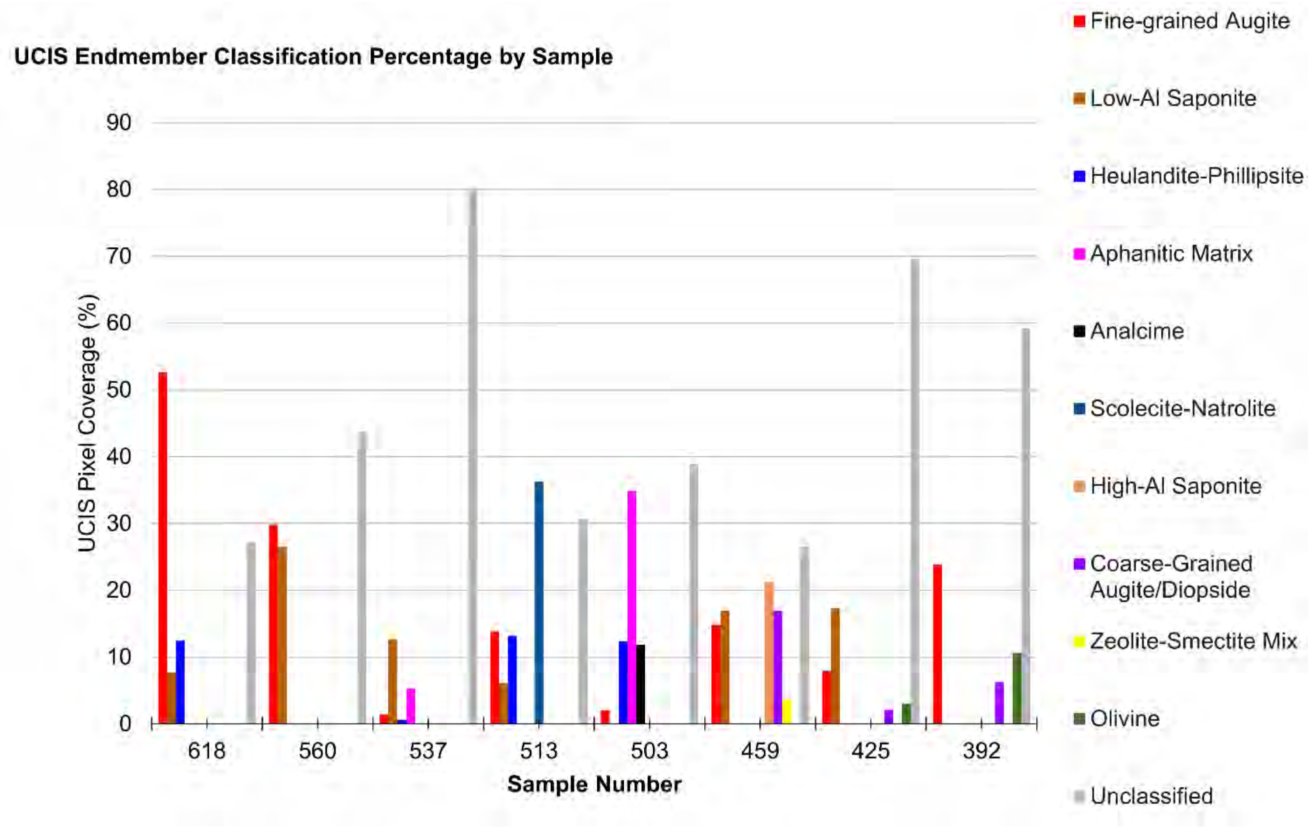

Appendix Figure 1

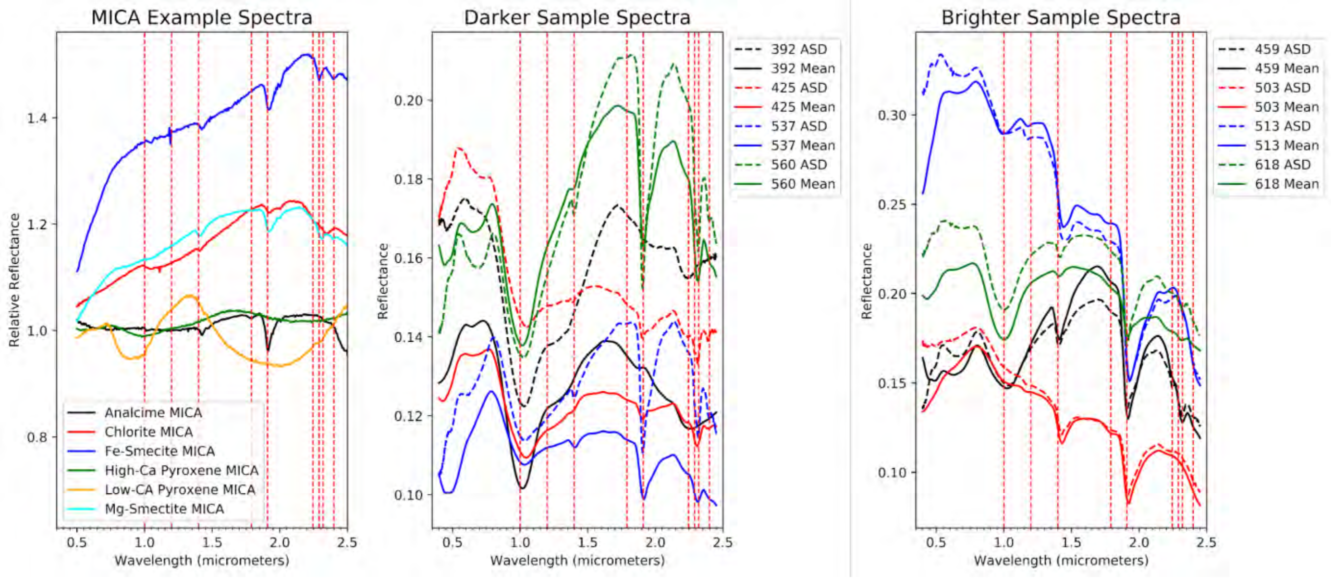

Appendix Figure 2

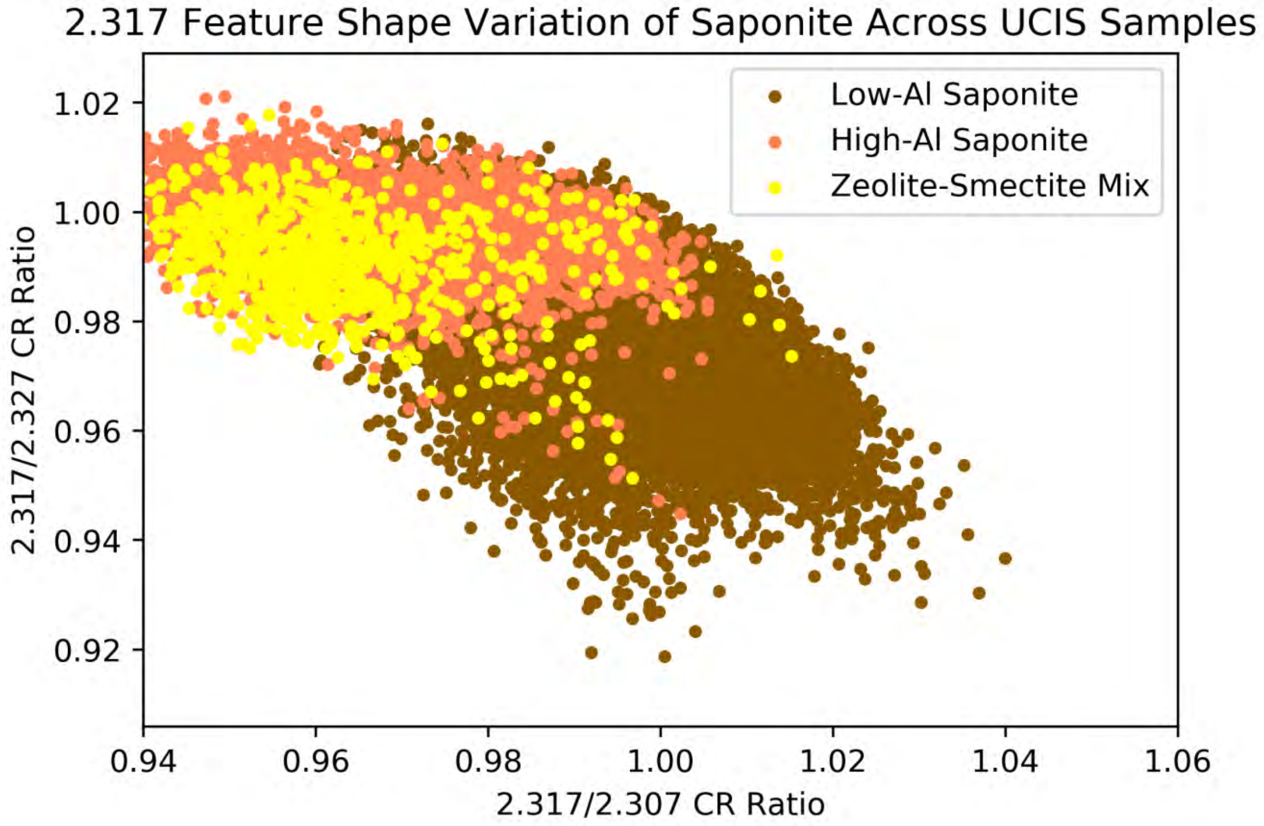

Appendix Figure 3

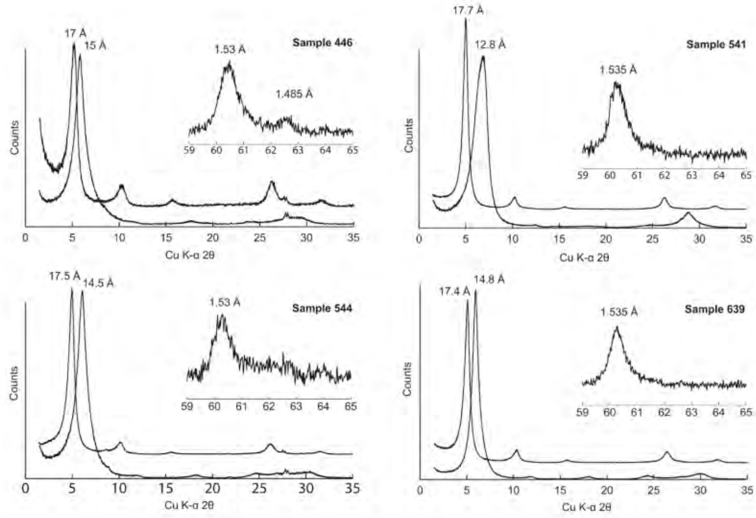

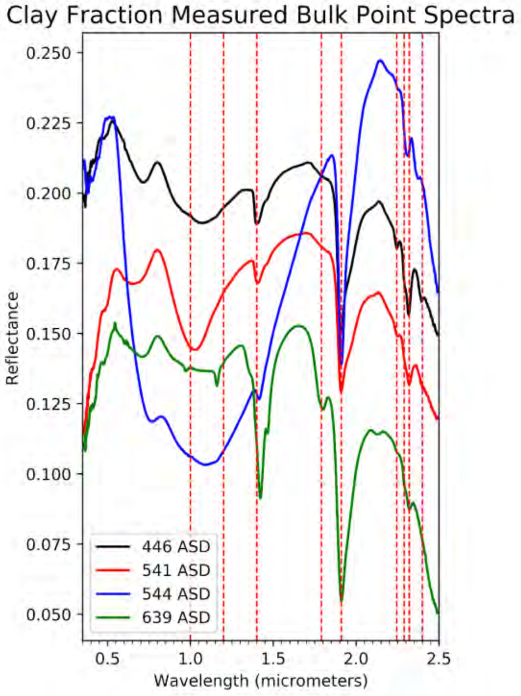

Appendix Figure 4